Turbulence Suppression at Extreme Plasma Densities on DIII-D and EAST

S. Ding[1*], A. M. Garofalo[1], H. Q. Wang[1], W. Choi[1], X. Z. Gong[2], J. P. Qian[2], J. Huang[2], D. Hatch[3], M. T. Kotschenreuther[3], S. Mahajan[3], D. B. Weisberg[1], Z. Y. Li[1], Z. Yan[4], X. Jian[2], S.-G. Baek[5], P. Bonoli[5], G. Wallace[5], D. Eldon[1], B. S. Victor[6], A. Marinoni[7], Q. M. Hu[8], I. S. Carvalho[1], T. Odstrčil[1], L. Wang[2], K. D. Li[2], A. W. Hyatt[1], T. H. Osborne[1], J. McClenaghan[1], C. T. Holcomb[6], J. M. Hanson[9], Y. X. Sun[2,10] and Z. H. Wang[2,10]

[1]General Atomics, P. O. Box 85608, San Diego, CA 92186-5608, USA
[2]Institute of Plasma Physics, Chinese Academy of Sciences, PO Box 1126, Hefei, Anhui 230031, China
[3]ExoFusion Inc., Bellevue, WA 98005-1805, USA
[4]University of Wisconsin-Madison, Madison, Wisconsin 53706, USA
[5]Plasma Science and Fusion Center, Massachusetts Institute of Technology, Cambridge, MA 02139, USA
[6]Lawrence Livermore National Laboratory, Livermore, California 94551, USA
[7]University of California San Diego, La Jolla, CA, 92093, USA
[8]Princeton Plasma Physics Laboratory, Princeton University, Princeton, NJ, 08543, USA
[9]Department of Applied Mathematics and Applied Physics, Columbia University, New York, New York 10027-6900, USA
[10]University of Science and Technology of China, Hefei, 230026, China
[*]Email: dingsiye@fusion.gat.com

Abstract: Recent high-poloidal-beta (high-β_P) experiments on DIII-D and EAST have made coordinated breakthroughs for high confinement quality at high density near the Greenwald limit. Density gradient amplification of turbulence suppression at high β_P can explain both of these achievements. Experiments on DIII-D have achieved Greenwald fraction (f_{Gr}=line-averaged density/Greenwald density) above 1 simultaneously with normalized energy confinement (H_{98y2}) around 1.5, as required in fusion reactor designs but never before verified in tokamak experiments with divertor configuration. A synergy between increased H_{98y2} and f_{Gr} is observed with strong gas puffing, due to the build-up of an internal transport barrier at large radius in the temperature and density channels. Transport simulations reveal that the favorable trend of reduced turbulent energy transport at higher density is only expected when increasing the density gradient at high local safety factor and high β, thus at high β_P to ensure strong α-stabilization. These conditions are crucial to many conceptual designs for steady-state reactors. New experiments on EAST have nearly doubled the ion temperature at f_{Gr}~0.9, consistent with predict-first modeling results based on the same physics revealed from the DIII-D analysis. All previous EAST long-pulse H-modes have $T_i << T_e$ near plasma axis. Transport modeling indicates that the profiles are limited by ion-temperature-gradient (ITG) modes at mid-radius. The modeling also suggested potential solutions, including reducing magnetic shear, enhancing density gradients and higher impurity concentration. Following this guidance, EAST experiments directly show a strong enhancement of T_i achieved with a combination of a 2nd plasma current ramp-up, a density gradient increase, and a Z_{eff} perturbation by a short pulse (100 ms) of impurity injection, as predicted by the earlier modeling.

1. Introduction

Economical fusion energy is being pursued world-wide via the tokamak approach by designing fusion pilot plants (FPPs) that aim at high fusion gain (Q=Fusion power / auxiliary power) and high fusion power [1-8]. Recent research indicates energy confinement quality (i.e., the extent to which H_{98y2} exceeds 1) is the highest leverage parameter for the capital cost of a compact tokamak FPP [6]. Designs with H_{98y2}>>1 significantly reduce the cost of an FPP. Two designs in the literature show that one with H_{98y2}=1.0 requires US$ 7.1 billion, while another with H_{98y2}=1.5 reduces the cost to US$ 4.5 billion. On the other hand, the thermonuclear power density is defined as $P=n^2\langle\sigma v\rangle E/4$, where n is the total fuel ion density with equal parts deuterium and tritium, $\langle\sigma v\rangle$ is the velocity averaged reactivity, and E is the energy released per reaction. When the ion temperature is above 14 keV, the change of $\langle\sigma v\rangle$ with temperature is relatively small in D-T fusion reactions [9]. The thermonuclear power density is proportional to fuel particle density squared. Therefore, high energy confinement quality and high fuel density are two key elements for economically attractive fusion. Most FPP designs require simultaneous f_{Gr} between 1 and 1.3, and H_{98y2} between 1 and 1.65 [1-8]. Here, f_{Gr} is Greenwald fraction, defined by line-averaged density ($\bar{n}_e$) over the Greenwald density (n_{Gr}~$I_p/\pi a^2$), where I_p is plasma current and a is minor radius. Note that the Greenwald density is recognized as a density limit for H-mode pedestal, not for core density [10].

However, the operational regime of simultaneous f_{Gr} between 1 and 1.3, and H_{98y2} between 1 and 1.65 is very difficult to demonstrate in present tokamaks. An ITPA database study for ITER Q=10 H-mode plasmas with carbon wall or with metal wall shows no experimental data with significant H_{98y2} above 1 at f_{Gr} above 1 (fig. 14 in [11]). Many dedicated high-density experiments have been performed in tokamaks [10]. The common finding is limited energy confinement quality ($H_{98y2} \leq 1$) at high density, near the Greenwald value. One example from DIII-D shows transient H_{98y2}~1 at f_{Gr}~1.4 by strong gas puffing [12]. Strong density peaking by large pinch velocity was observed. In another example, ASDEX Upgrade achieved transient f_{Gr}~1.5 by pellet injection [13, 14]. Unfortunately, decreased stored energy was observed in this experiment at high density, resulting in H_{98y2} below 1.

Likely the only previous H-mode experimental result in the literature which is close to the attractive FPP operational regime of simultaneous f_{Gr} ~ 1 - 1.3, and H_{98y2} ~ 1 - 1.65, is from JT-60U [15]. Reversed shear (RS) plasmas in JT-60U achieved simultaneous $f_{Gr} \geq 1.0$ and $H_{98y2} \geq 1.0$. Two best examples are f_{Gr}=1.09, H_{98y2}=1.3 and f_{Gr}=1.18, H_{98y2}=1.15. However, impurities seem to play a role in the achievements, leading to high Z_{eff} (>4) and strong radiation. The neutron rate does not increase with higher line-averaged density (it decreases in some cases). This suggests a strong contribution of impurities to the increased electron density. Other than H-mode, it is also worthwhile to mention the radiative improved mode (RI-mode) in TEXTOR tokamak, which was reported achieving H_{98y2}>1 and f_{Gr}>1 with impurity injection [16]. Note that this result was obtained in a circular tokamak with a limiter configuration and an L-mode edge. Recent negative triangularity experiments on DIII-D also show remarkable progress on achieving H_{98y2}~1.05 and f_{Gr}>1 at the same time without having a significant pedestal pressure [17].

A recent breakthrough in extending the operational space of tokamak experiments with divertor configuration has been reported in DIII-D [18], leveraging the high-poloidal-beta (high-β_P) advanced scenario [19-23]. β_P is defined by the ratio of volume-averaged plasma pressure to the pressure of the poloidal magnetic field contributed by the toroidal current in the plasma. Sustained plasmas with simultaneous high energy confinement quality (H_{98y2}~1.3-1.8), high density ($1<f_{Gr}\leq 1.25$), small ELMs and reduced divertor heat load are achieved in the DIII-D high-β_P experiments, without use of impurity injection. Transport modeling based on a high-β_P experimental equilibrium shows reduced turbulent

transport at higher density, which is consistent with the observation of synergy between the increasing H_{98y2} and the increasing f_{Gr} in the experiment. Transport modeling further indicates that the favorable conditions for accessing such transport regime are relatively high local q and high β, i.e. sufficient α_{MHD} at high β_P. Here, q is safety factor, β is ratio of volume-averaged plasma pressure to the pressure of the toroidal magnetic field (B_T) and α_{MHD} is normalized pressure gradient defined by $-q^2/B_T^2 R dp/dr$, where p is plasma pressure, R is major radius and r is minor radius. One of the goals of this paper is to provide extended analysis and details of the high density high confinement experiments on DIII-D and the related transport modeling.

Another goal of this paper is to report improved confinement in EAST high-β_P plasmas at density close to the Greenwald value, both from predict-first modeling and experimental tests. EAST has achieved 403 s long pulse operation with β_P~2.5 and f_{Gr}~0.7 using only radio frequency power [24]. However, there are scientific challenges in these EAST high-β_P plasmas. One challenge is that, even with similar q_{95} (6.5-11) and β_P (1.95-3.0) compared with DIII-D high-β_P plasmas, the internal transport barrier (ITB) forms at small radius (e.g. ρ<0.3) and only in the electron temperature profile. Here, ρ is the square root of the normalized toroidal magnetic flux, a normalized minor radius coordinate. This results in relatively small improvement in the stored energy, due to only improved T_e in small core volume. An important goal of the joint DIII-D/EAST research on high-β_P scenario development is to develop an ITB at large radius, e.g. ρ~0.6-0.7 as shown in the DIII-D discharges [23]. This requires a deep understanding of the governing physics in the DIII-D results and also an application of the same physics in EAST experiment. Although the goal has not been fully achieved yet, there are some progress to be reported in this paper, regarding the limiting facts on EAST and some potential solutions based on transport modeling results. Another challenge is that the on-axis ion temperature ($T_{i,0}$) in the EAST high-β_P plasmas is usually limited around 1.0 keV, much lower than the on-axis electron temperature ($T_{e,0}$), which is usually above 4 keV [24]. This is a long-standing limitation for the EAST long-pulse high-β_P plasmas. This paper presents results of modeling studies aimed at understanding the physics that limits the performance of the EAST high-β_P plasmas, and at providing guidance towards overcoming those limitations. The result of nearly doubled $T_{i,0}$ at f_{Gr}~0.9 in recent EAST high-β_P experiments which followed the modeling guidance will also be discussed.

The rest of this paper is organized as following. Experiments and modeling results from DIII-D are described in section 2. EAST transport modeling results and the latest high-β_P experiments to test the proposed approaches are shown in section 3. Section 4 summaries the results reported in this paper.

2. DIII-D experiments and modeling results

2.1 DIII-D database for discharges between 2019 and 2023

A DIII-D database on experimental H_{98y2} and f_{Gr} has been created based on the experiments performed between 2019 and 2023 (fig. 1). More than 4200 discharges are included with the following constraints. Each discharge contributes pairs of (f_{Gr}, H_{98y2}) from two time slices: 1) highest H_{98y2} and the corresponding f_{Gr}; (2) highest f_{Gr} and the corresponding H_{98y2}, unless the two time slices are the same. $I_p \geq 0.55$ MA, $dI_p/dt < 0.5$ MA/s, $P_{tot} \geq 5$ MW, $W \geq 500$ kJ and $(dW/dt)/P_{tot} \leq 0.1$. Here, W is the total stored energy of plasma, and P_{tot} is total heating power. A smoothing window of 40 ms is applied to the data as well. Only H_{98y2}

values between 0.5 and 2.5 are considered. Note that this is an updated version of the database discussed in the previous publication [18].

Fig. 1 clearly indicates that the high-β_P scenario has extended the operational space in DIII-D experiments towards a high-f_{Gr} and high-H_{98y2} regime, which is required by many attractive FPP designs as mentioned in the introduction of this paper. The corner space of "attractive FPP design" represents a collection of required H_{98y2} and f_{Gr} for desired fusion gain and fusion power from previous FPP designs [1-8]. Impurity (neon) seeding was used in the 2019 high-β_P experiments as our first attempt to push the operational boundary [23]. This approach was successful, as one can see from the red diamonds in fig. 1. However, progress was limited by the strong neon injection into the plasma causing high radiated power for the core, up to 60% of the injected power. This limited the achievable H_{98y2}. Also, the impurity injection complicates the physics understanding of the operational achievements, as impurity injection itself is considered as an effective approach to suppress turbulent transport in tokamak plasmas [25]. Along this line, it is all the more remarkable that experiments without impurity injection in 2022 achieved even higher H_{98y2}, as shown by the blue squares in fig. 1. This result is a main focus of this paper. Since no impurity injection was used, the 2022 experimental results suggest that impurity turbulence suppression may only have played a minor role in the high confinement quality of the earlier high-β_P scenario experiments. Note that fig. 1 shows a few non-high-β_P data points with H_{98y2}~1.05 and f_{Gr}>1.0. They are from negative triangularity experiments [17]. Also note that the work described in this paper does not attempt to produce discharges with high absolute performance, but to produce discharges that can access the reactor-relevant and underexplored parameter space with simultaneous H_{98y2}>1 and f_{Gr}>1.

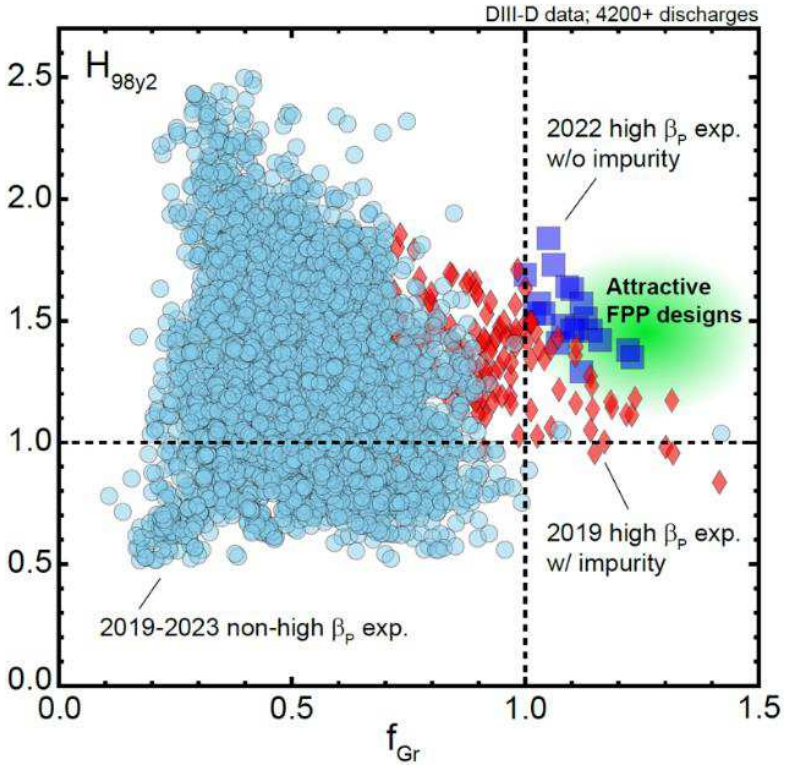

Fig. 1 Database of H_{98y2} and f_{Gr} on DIII-D discharges. More than 4200 discharges are included. Red diamonds show high-β_P experiments in 2019 with impurity injection. Blue squares are the high-β_P experiments in 2022 without impurity. Cyan circles represent all other experiments in 2019-2023. Shaded area in green indicates the parameter space for attractive FPP designs. Vertical and horizontal dashed lines show f_{Gr}=1.0 and H_{98y2}=1.0, respectively.

2.2 DIII-D High-β_P discharge #190904 with simultaneous f_{Gr}>1 and H_{98y2}~1.5

A typical DIII-D high-β_P discharge (# 190904) from the 2022 data set in fig. 1 has been discussed in details in [18]. In order to minimize overlap with the previous publication, a brief summary is presented in this subsection and readers should refer to the fig. 2 and the extended data fig. 1 in [18] for detailed information of time histories and profiles.

A striking feature of this discharge is the increasing H_{98y2} and the increasing f_{Gr} at the same time, which is unlike observations in most high-density H-mode experiments as mentioned in the introduction section. This discharge achieves simultaneous f_{Gr}~1.15 and H_{98y2}~1.5. The high-density and high-confinement phase with f_{Gr}>1.0 and H_{98y2}>1.0 in this discharge is sustained for about 2.2 s, i.e. 2.2×τ_R or 24×$\tau_{E,th}$, where τ_R is the current diffusion time and $\tau_{E,th}$ is the thermal energy confinement time of the plasma. The termination of this phase is due to neutral beam injection (NBI) power ramp-down. β_N~3.5 and β_P~2.9 have been achieved. The key reason of achieving high energy confinement quality and high density is establishing ITBs at large radius in temperature and density channels. Fig. 2 shows typical temperature and density profiles in this discharge, along with the calculated electron/ion heating sources, electron particle source, electron/ion thermal diffusivities and electron particle diffusivity from TRANSP code [26] during a multi-step workflow "kinetic EFIT reconstruction" [27]. One can see a very clear feature of ITB -- significantly reduced thermal and particle diffusivities in a layer at ρ~0.7 with a radial width around 0.2-0.3 in ρ. The region with reduced diffusivity coefficients is associated with the measured steep temperature/density profiles. Note that a smooth procedure with a window of ρ=0.03 has been applied on the thermal diffusivity plots.

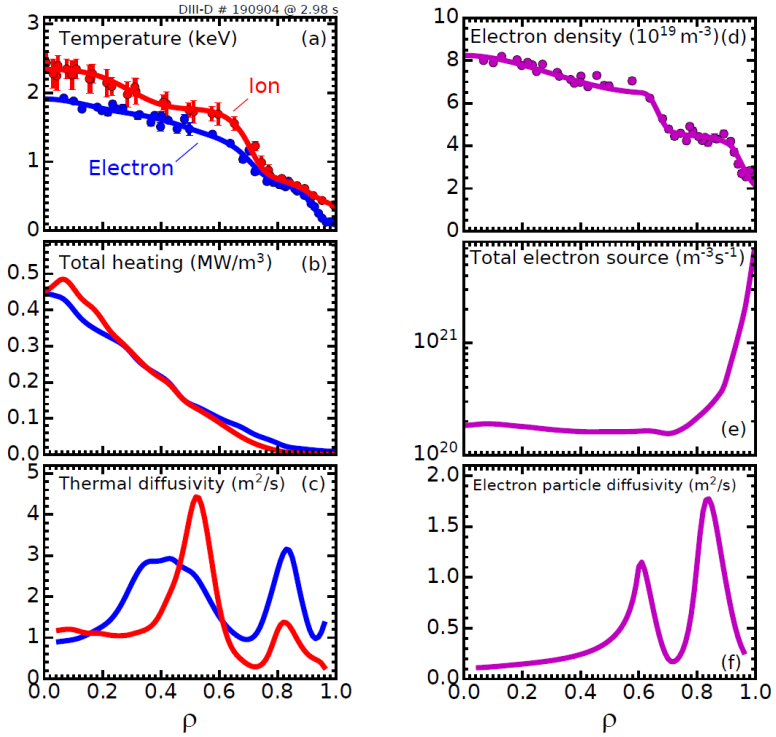

Fig. 2 Profiles of DIII-D #190904 at 2.98 s. (a) Electron temperature in blue; Ion temperature in red; (b) Total electron heating in blue; Total ion heating in red; (c) Electron thermal diffusivity in blue; Ion thermal diffusivity in red; (d) Electron density; (e) Total electron source; (f) Electron particle diffusivity.

While D_2 gas puffing under feedback control is applied through this discharge, a feedforward D_2 gas puffing from low field side is added from 2.8 s. This approach ensures sufficient particle source into the plasma, regardless of the change in the feedback source. Note that the gas puffing feedback is set to control the pedestal electron density in this discharge. An alternative approach is setting a non-zero minimum D_2 gas puffing rate with feedback control, if no additional gas value is available. In this discharge, the on-axis electron density reaches Greenwald fraction $f_{Gr,0}$~1.4, while the pedestal electron density remains at $f_{Gr,ped}$~0.7, i.e. 4×10^{19} m^{-3}. There is very little change in pedestal pressure, corroborating the beneficial effect of the large radius ITB on the observed confinement level. Puffing D_2 not only increases the electron density above the Greenwald value, but also increases the deuterium density. Meanwhile, the electron and ion temperatures also increase at almost constant injected power. $\tau_{E,th}$ increases with density as well, from 47 ms at f_{Gr}~0.7 (t~2.0 s) to 96 ms at f_{Gr}~1.15 (t~4.7 s). One can imagine the very promising application of this operational scenario in an FPP – simultaneous increase of n_i, T_i and $\tau_{E,th}$, all three components in the triple-product. The measured neutron rate, which can serve as an indicator of fusion performance, increases substantially, about 67% higher (from 0.6×10^{15} s^{-1} to 1.0×10^{15} s^{-1}), while the injected power slightly decreases. T_i/T_e in this discharge is relatively close to the FPP condition. The ratio in high density phase, e.g. 4.78 s, is between 1.14 and 1.6 for all radii inside ρ=0.95. There are experimental observations in international tokamaks on reduced plasma performance or confinement quality at high electron density at separatrix (n_{sep}) or its Greenwald fraction (n_{sep}/n_{Gr}) [28, 29]. However, the high-β_P discharge reported in this paper shows a different trend. One can find increased H_{98y2} together with increased n_{sep} in fig. 2 of [18]. $\tau_{E,th}$ vs n_{sep} also shows the same trend. n_{sep}/n_{Gr} ranges from 0.1 to 0.5 in this discharge. Although some of the quantities (e.g. H_{98y2}, densities, β_N, etc.) show a potential trend of saturation, it is not entirely sure if the plasma is approach a stationary state or it would continue to evolve to a lower-stability state, due to the limited pulse length on DIII-D. Actively controlled heating power and fueling rate are important to future experiments that reproduce this plasma in a longer time scale.

The issue of impurity accumulation is a usual concern in an ITB plasma. In this discharge, the main impurity, carbon, is observed to develop its own density ITB at large radius as well. However, the profile is not strongly peaked on axis. The difference between the measured carbon density (n_C) profiles and a predicted profile by neoclassical transport (e.g. fig. 4(d) in [30]) can be easily identified. The ratio of measured n_C/n_e is kept to about 4-5% during the discharge evolution. This is also consistent with the well-controlled core radiated power. The fraction of injected power that is radiated from the core is about 10-20%. Therefore, no core impurity accumulation has been observed during the $24\times\tau_{E,th}$ duration of the high-density ($f_{Gr}\geq1.1$) and high-confinement (H_{98y2}~1.5) phase. Safety-factor (q) profile is self-organized during the formation of strong ITBs at large radius. There is a small well in the q-profile at large radius, aligning with a weak ITB at early time slice. The q-profile well becomes larger, which is associated with large local bootstrap current density by the gradients of a strong ITB, at a later time slice. The local minimum q (q_{min}) in the outer half of the plasma is located at ρ~0.6 for a duration of about $2\times\tau_R$. q_{min} in this discharge is maintained above 2. Note that the deuterium densities and q-profiles are not direct measurements. Kinetic EFIT reconstruction is used to calculate these quantities based on magnetic equilibria reconstructed with improved accuracy by adding pressure and plasma current density constraints.

We have observed reduced turbulence fluctuations at high density in the analyzed DIII-D discharge #190904. Three turbulence measurements taken from the Beam Emission Spectroscopy (BES) system [31] at different density levels are shown in fig. 3(a). Each measurement uses a time-windows of 300 ms and

the time slices for the measurements are indicated in fig. 3(b) with vertical shaded bands. The radial location of the measurements is around ρ=0.6. Note that the data come from two fixed BES channels in R-Z panel. Due to the growing ITB, the two BES channels move deep into ITB region gradually as one can find the increasing α_{MHD} (proportional to pressure gradient) shown in fig. 3(b). Counter-intuitively, higher pressure gradient does not drive stronger turbulence, but correlates with measurements of lower turbulent fluctuations: gradually reduced long wavelength (0.1-0.2 cm^{-1}) density fluctuations from relatively low density (f_{Gr}~0.76) to high density (f_{Gr}~1.1). This is consistent with the increased H_{98y2} and the increased $\tau_{E,th}$ from 50 ms to 90 ms. Similar to the increasing f_{Gr}, the local electron density at ρ=0.6 increase as well (fig. 3(b)), when turbulence is gradually suppressed and α_{MHD} increases. Beyond a simple correlation, it is believed that α-stabilization on turbulent transport is the governing physics behind the experimental achievement [18]. Enhanced α-stabilization at higher density gradient has been proposed by theoretical studies [32] and will be discussed in section 2.5 of this paper. The BES measurements provide experimental evidences in support of the α-stabilization physics in the high-β_P scenario by showing lower turbulent fluctuation at higher α_{MHD}, i.e. higher normalized pressure gradient.

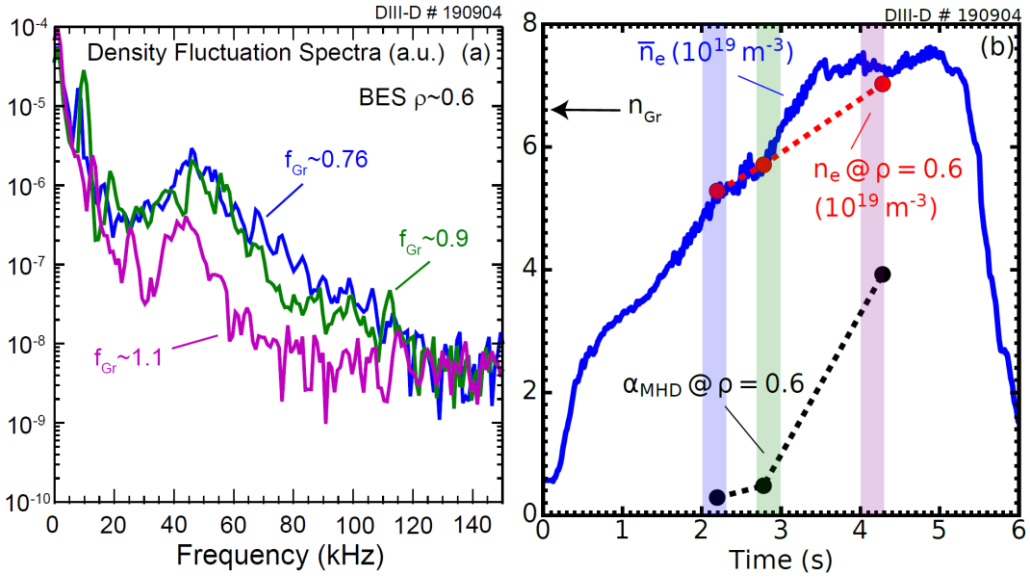

Fig. 3 (a) Spectra of density fluctuations in DIII-D #190904 at ρ~0.6, measured by the BES diagnostic system. Relatively low density (f_{Gr}~0.76) case is shown in blue. Medium density (f_{Gr}~0.9) case in green, and high density (f_{Gr}~1.1) case in magenta. The colors align with the shaded areas in (b), showing when the measurement is taken; (b) Time history of line-averaged n_e in blue; n_e at ρ=0.6 in red; α_{MHD} at ρ=0.6 in black.

2.3 High confinement quality at reduced toroidal rotation in the high-β_P discharge #190904

High toroidal rotation and the associated high E×B shear is one of the more common physics mechanisms that suppress turbulent transport and lead to improved energy confinement in tokamak plasmas [33]. This subsection is dedicated to discussing the observation of achieving high energy confinement quality at reduced toroidal rotation in the high-β_P discharge #190904.

Mixed co- and counter-I_p NBI is used in #190904. The injected NBI torque is about 5-6.5 N-m in this discharge, for a power level of 10-12 MW. Note that all co-I_p NBI on DIII-D usually has injected torque of 8-10 N-m at this power level, and higher NBI power usually gives higher torque. Clearly, the plasma density

also plays an important role in the effectiveness of the external torque at driving toroidal rotation. The experimental measurements indicate a gradually reduced torque per particle (fig. 4(b)) between 1.2 s and 3.3 s, and gradually reduced difference in toroidal rotation between plasma core and pedestal in the same period of time (fig. 4(c)). The toroidal rotation is measured by a multi-channel CER diagnostic [34]. The core and pedestal channels used here are located at ρ~0.2 and 0.9, respectively. A large difference in toroidal rotation between plasma core and pedestal can serve as a general indicator of large toroidal rotation contribution to core E×B shear. Interestingly, the evolution of H_{98y2} is anti-correlated with the evolution of both torque per particle and core-pedestal rotation difference after 2.0 s. To compare with the dependence of H_{98y2} on the toroidal rotation discovered in other scenarios [35, 36], the evolution of H_{98y2} in #190904 between 1.3 s and 4.86 s has been plotted in fig. 4(d) against the core toroidal rotation at ρ~0.2 and the pedestal toroidal rotation at ρ~0.9. In general, the dependence shown in this high-β_P discharge suggests higher H_{98y2} at lower toroidal rotation, which is an opposite trend to most results in the literatures, but favorable for an FPP. $\tau_{E,th}$ is behaving the same as H_{98y2}. Toroidal rotation profiles at early and later time slices are displayed in fig. 4(f), showing lower toroidal rotation at all radii when having ITB. However, the presence of large radius ITB elevates the core toroidal rotation, which in turn can be helpful on both transport and MHD stability at low input torque. The increased local rotation shear around ρ~0.6, even as the rotation is overall decreasing, may contribute to turbulence suppression as well. The calculated total torque densities, which consider collisional torque, J×B torque, etc. in the power balance calculations, are shown in fig. 4(e) as well for the same time slices. One can see that the effective torque density is lower in the core at early time slice. But it leads to higher toroidal rotation, probably because of relatively low density (low moment of inertia). Torque density increases at later time because of higher co-NBI power in the high β_N phase.

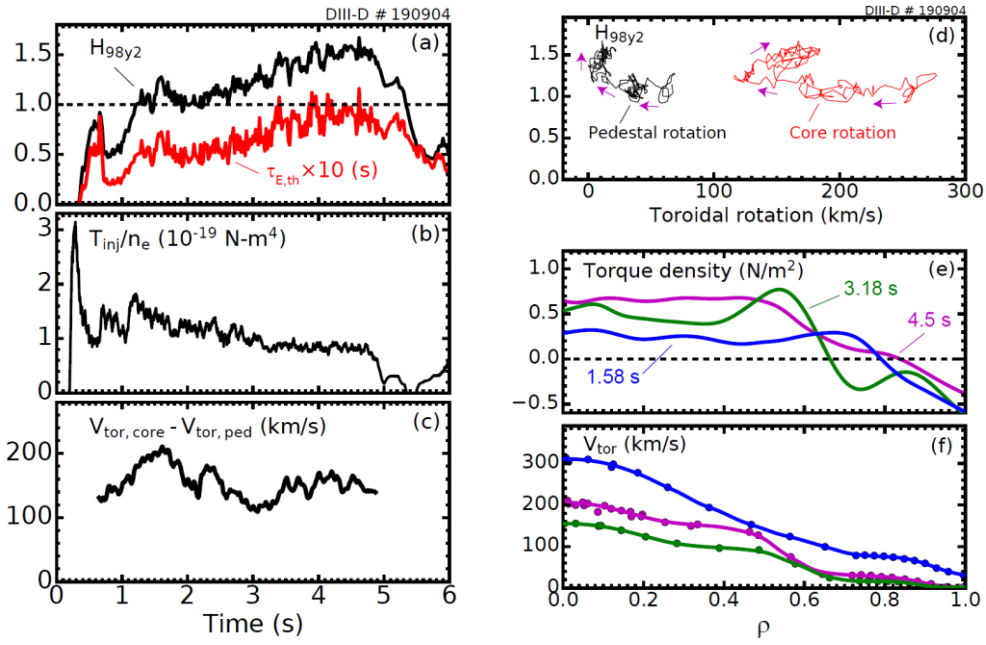

Fig. 4 Time histories of experimental parameters of DIII-D #190904: (a) H_{98y2} in black; thermal τ_E in red; (b) NBI torque per particle; (c) Difference of toroidal rotation between plasma core (ρ~0.2) and pedestal (ρ~0.9). (d) H_{98y2} vs toroidal rotation. Data from 1.3 s to 4.86 s are included. Core rotation in red, pedestal rotation in black. Magenta arrows show the flow of time; (e) Total input torque density; 1.58 s in blue, 3.18 s in green and 4.5 s in magenta; (f) Toroidal rotation profiles; same color coding as (e); Dots indicate measurements.

2.4 Different dependence of H_{98y2} on $\bar{n}_e$ between a high-β_P discharge and a low-q_{95} H-mode discharge

In order to better understand the unique features of the core energy transport at high density in the high-β_P scenario, high-β_P discharge #190904 (discussed in the previous subsections) is compared in this section with a typical DIII-D low-q_{95}, high-density H-mode, discharge #187019. Some experimental waveforms of these two discharges are plotted in fig. 5. Between 2.0 s and 5.0 s, these two discharges have almost the same injected power (fig. 5(b)) and similar high density, above 5×10^{19} m^{-3} (fig. 5(d)). The outstanding differences lie in the plasma current and the resulting q_{95} as shown in fig. 5(a). Discharge #187019 has I_p at 1.3 MA and q_{95} at 4.2, while discharge #190904 has I_p at 0.73 MA and q_{95} at 8.5. As will be further elucidated later in this paper, the resulting difference in local q value at large radius plays an important role in accessing the low transport regime at high density.

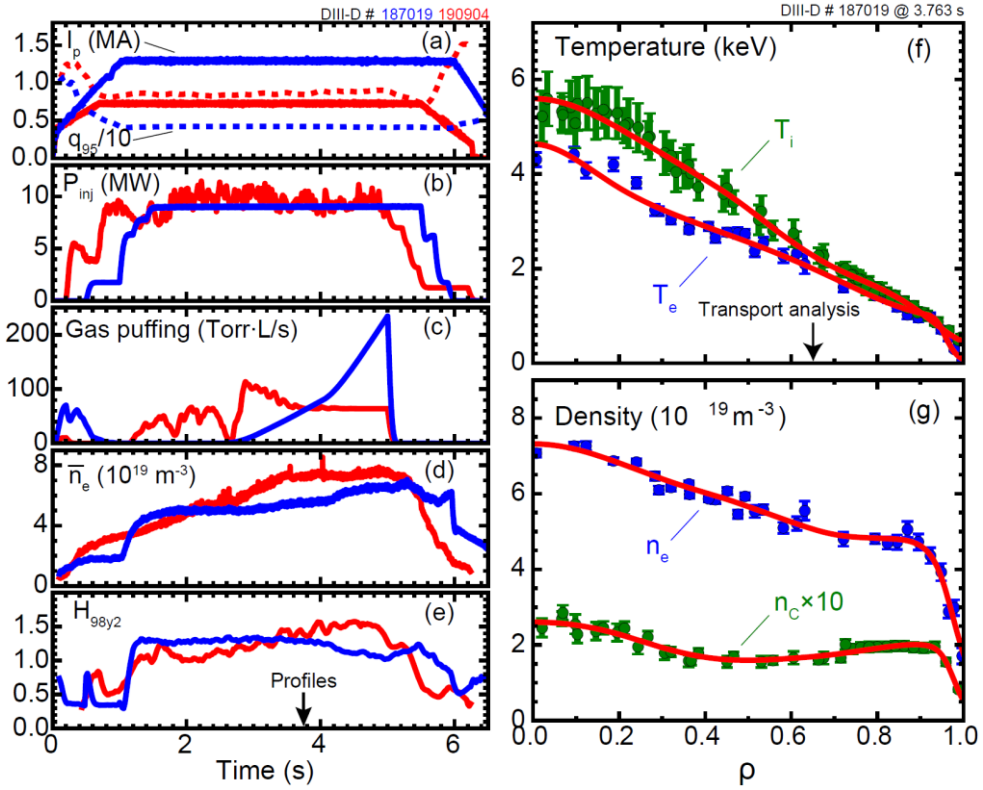

Fig. 5 Experimental waveforms of DIII-D discharges #187019 (blue) and #190904 (red). (a) Plasma current I_p in solid lines; Safety factor q_{95} in dashed lines; (b) NBI power; (c) Total gas puffing rate; (d) Line-averaged density; (e) Global energy confinement quality. (f)-(g) profiles from #187019 at 3.763 s. (f) Electron temperature in blue circles; Ion temperature in green circles; (g) Electron density in blue circles; Carbon (impurity) density in green circles; In (f) and (g), red solid lines are the profile fits of the experimental data; Black arrows in (e) and (f) indicate the time slice for profiles and the radial location for transport analysis, respectively.

The gas puffing trajectories in the two discharges are also different (fig. 5(c)). After 4.0 s, #187019 uses very large gas puffing rate to approach high density, which implies a deteriorating particle confinement. As for energy confinement quality, both discharges have quite high values, e.g. H_{98y2} >1.2, but in different phases (fig. 5(e)). #187019 has higher H_{98y2} at lower density, while #190904 has higher H_{98y2} at higher density. The different trend on H_{98y2} vs $\bar{n}_e$ can be seen more clearly in fig. 6. The decreasing trend shown in #187019 is actually consistent with observations in most of the high-density H-mode experiments

worldwide, as discussed in the introduction section. The increasing trend in #190904 is clearly more favorable for FPPs. In the next subsection, transport analysis will show lower turbulent transport in #190904 and higher turbulent transport in #187019, when increasing the core density gradient. Note that the major goal of this analysis is not to fully understand the physics (maybe multiple contributing effects) behind the trend of decreasing confinement in this particular discharge #187019, but to reveal that a general challenge of increased turbulent transport can be explained from core transport analysis alone (no effects of pedestal, fast ion, etc. involved).

The temperature and density profiles of #187019 from 3.763 s are shown in figs. 5(f) and 5(g). One can see the typical standard H-mode profile shape in each channel, clearly different from the ITB-type profiles shown for the high-β_P case in fig. 2. The transport analysis for #187019 in the next subsection uses the profiles shown in fig. 5 and the corresponding reconstructed equilibrium.

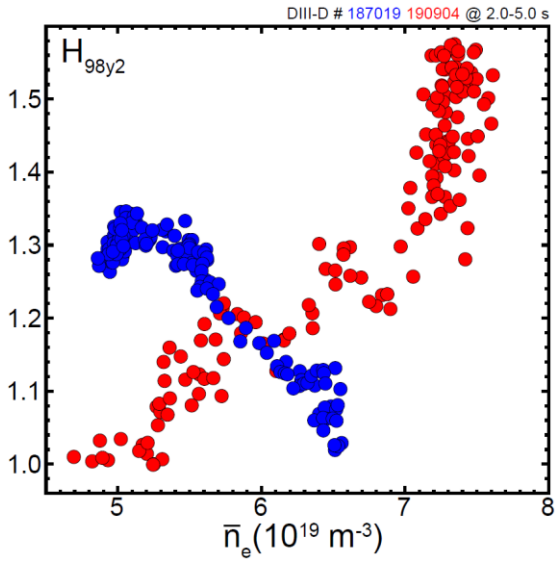

Fig. 6 H_{98y2} vs $\bar{n}_e$ for discharges #187019 (blue) and #190904 (red) between 2.0 s and 5.0 s.

2.5 Different features of turbulent transport at higher density gradient

The Gyro-fluid transport code TGLF [37] has been employed to explore the physics behind the experimental observations of the different dependences of H_{98y2} on $\bar{n}_e$ discussed above. The saturation rule SAT-2 [38] with electromagnetic effects enabled is used in this TGLF modeling. For all experimental kinetic equilibria, the modeling focuses on a radial location at ρ=0.65. The analysis takes the contributions from multiple turbulent modes (low-k and high-k) into account, and the turbulent heat fluxes are predicted. The key approach in this modeling is to scan F_p, which is the fractional contribution of the density gradient to the pressure gradient, defined by $F_p=T\nabla n/\nabla p=1/(1+\eta)$. Here, $\eta=L_n/L_T=n\nabla T/T\nabla n$. When scanning F_p, quasi-neutrality is kept, meaning the density gradients for all species will change accordingly. The main purpose of this approach is to test the plasma response (turbulent transport) to the change of density gradient at mid-radius. At first, this subsection will focus on answering the following questions: 1) What does the transport model predict when the core density gradient is increased in the high-β_P cases, since the experimental observations show higher H_{98y2} and reduced turbulence at higher density? 2) How is the prediction different for the low-q_{95} H-mode case, where the experimental observations show lower H_{98y2} at higher density?

For the high-β_P discharge #190904, two time slices with different α_{MHD} values are chosen. One is relatively low α_{MHD} of 1.13 at 2.78 s, and the other is high α_{MHD} of 2.75 at 4.28 s. The TGLF parameters used in the simulations are listed in table 1. As shown in fig. 7(a), F_p scans in both cases suggest decreased turbulent energy transport at higher F_p. It is important to notice that the turbulence suppression effect is much stronger at high α_{MHD}. In the results, the predicted Q_e is normalized by the gyro-Bohm heat flux ($Q_{GB}=n_e c_s T_e(\rho_s/a)^2$). Here, c_s is sound speed $\sqrt{T_e/m_i}$, and ρ_s is ion sound gyro-radius $c_s/(eB_T/m_i)$, where e is electron charge and m_i is ion mass. The modeling results reveal the important feature of the high-β_P scenario that anomalous turbulent transport can be reduced at higher density gradient or higher core density with similar pedestal density. The results are consistent with the experimental observations of reduced turbulent fluctuations and increased H_{98y2} in the high-β_P experiment discussed above. The key physics that leads to the unique feature is α-stabilization of turbulent transport at high density gradient as discussed in [18]. Note that there are two numerical approaches to vary F_p in the scan: constant ∇T or constant ∇p. Results using both approaches are presented in fig. 7(a) with experimental collisionalities and they show consistent trends. Also, similar results are obtained for the ion energy transport. As one may know, collisionality is controlled by a separate variable in TGLF. Therefore, collisionality is kept unchanged in each F_p scan. Dedicated tests with lower collisionalities (10% of the experimental values) based on these equilibria are performed. The results (solid dots in fig. 7(a)) show the same trend as discussed previously and suggest that the same physics of turbulence suppression can be applied to lower collisionality.

Table 1 Major TGLF input parameters of DIII-D cases in subsection 2.5

Case	ZS_1	MASS_1	RLNS_1	RLTS_1	TAUS_1	AS_1
#190904 at 2.78 s	-1	0.000272	1.28	0.603	1	1
#190904 at 4.28 s	-1	0.000272	4.058	7.064	1	1
#187019 at 3.763 s	-1	0.000272	0.726	2.086	1	1
Case	ZS_2	MASS_2	RLNS_2	RLTS_2	TAUS_2	AS_2
#190904 at 2.78 s	1	1	0.598	1.404	1.187	0.785
#190904 at 4.28 s	1	1	3.312	4.025	1.339	0.808
#187019 at 3.763 s	1	1	0.989	2.564	1.14	0.755
Case	ZS_3	MASS_3	RLNS_3	RLTS_3	TAUS_3	AS_3
#190904 at 2.78 s	6	6	3.764	1.404	1.187	0.0326
#190904 at 4.28 s	6	6	7.426	4.025	1.339	0.0293
#187019 at 3.763 s	6	6	-0.611	2.564	1.14	0.0332
Case	RMIN_LOC	RMAJ_LOC	BETAE	P_PRIME_LOC	Q_PRIME_LOC	Q_LOC
#190904 at 2.78 s	0.684	2.96	0.00299	-0.00445	-34.76	5.1
#190904 at 4.28 s	0.672	2.947	0.00318	-0.0148	-10.29	3.73
#187019 at 3.763 s	0.715	2.919	0.004	-0.0034	10.898	2.118
Case	XNUE	ZEFF	VEXB_SHEAR			
#190904 at 2.78 s	0.133	1.978	0.0642			
#190904 at 4.28 s	0.194	1.878	0.0955			
#187019 at 3.763 s	0.649	1.996	0.0799			

Using an equilibrium reconstruction of the low q_{95} H-mode discharge #187019 at 3.763 s, TGLF modeling with the same approach gives an opposite dependence. The TGLF input parameters of this case are also listed in table 1. The prediction shows higher turbulent transport at higher F_p (fig. 7(b)), implying worse energy confinement at higher core density. Again, this is consistent with the experimental observation in the low-q_{95} H-mode discharge during the higher density phase. Lower collisionality does not change the

trend. Although the dependence of transport on F_p is opposite in the two types of discharge, the TGLF modeling is able to qualitatively predict both trends. One may be wondering what the dominant turbulent instability would be in the low-q_{95} H-mode case at mid-radius. TGLF suggests a low-k ion mode with ballooning type eigen-function. In a dedicated test, T_i gradient is observed to be a major drive of this mode, while the response to T_e gradient is very week. Artificially increasing local q from the experimental value 2.1 to 5.1 does not change the dominant turbulence. According to these features, this mode is likely to be the ion temperature gradient (ITG) instability. On the other hand, TGLF predicts electron modes at low-k ($k_\theta\rho_s$<1.0) in the high-β_P cases.

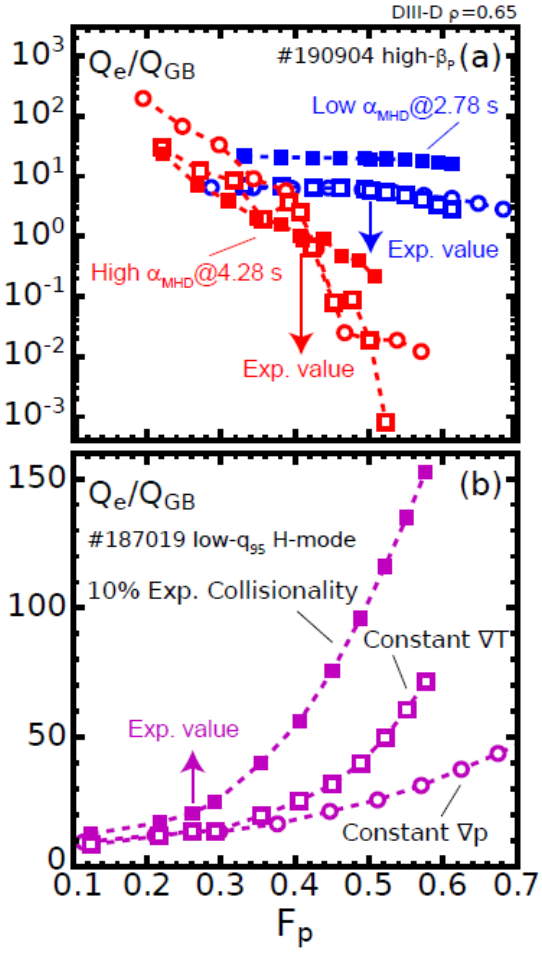

Fig. 7 Normalized predicted electron turbulent heat fluxes (Q_e/Q_{GB}) vs F_p calculated by TGLF at ρ=0.65 based on the reconstructed experimental equilibria. (a) High-β_P discharge #190904; The relatively low α_{MHD} case from 2.78 s in blue and the high α_{MHD} case from 4.28 s in red; (b) Low-q_{95} H-mode discharge #187019. Predicted Q_e/Q_{GB} in each experimental condition is highlighted by arrows. Squares show scans with constant ∇T, and circles represent scans with constant ∇p. Open symbols indicate results with experimental collisionality, and solid squares show results with 10% of experimental collisionality.

A natural next question is whether the low-q_{95} H-mode equilibrium can access the favorable low turbulent transport, high density regime and what the key parameters might be. To answer this question, 2D scans (F_p and another quantity) were performed using TGLF and the results are illustrated partially in fig. 3 of [18] and partially in fig. 9 in this paper. The first quantity we investigated is local q at mid-radius, since q

value is one of the major differences between the two cases discussed above. When scanning local q, other quantities in TGLF that are not independent from q, are scanned accordingly. That includes 'P_PRIME_LOC' and 'Q_PRIME_LOC', where P_PRIME_LOC is defined as $\frac{qa^2}{rB_{\text{unit}}^2}\frac{\partial p}{\partial r}$ and Q_PRIME_LOC is $\frac{q^2a^2}{r^2}s$. Here, q is local q, B_{unit} is a normalized toroidal field calculated and used in TGLF internally, and s is magnetic shear. In order to reduce overlap with the previous publication, readers should refer to fig. 3 in [18] for the 2D scan results of the normalized electron turbulence flux Q_e/Q_{GB} on local q and F_p. The results suggest a dependence reversal of Q_e/Q_{GB} on F_p at different local q. At low local q, where the experimental data point stays, turbulent transport increases at high F_p. This is consistent with the 1D scan in fig. 7(b). At medium q, transport at high F_p is more or less similar to the transport at low F_p. But at high q, the low turbulent transport area is found at high F_p. This regime has similar feature of transport as shown in fig. 7(a) based on the high-β_P experimental data. This may be related to the stronger α-stabilization effect at high q due to the fact that α_{MHD} is proportional to q^2. A threshold value of local q (q_{thr}) that enables such regime, can be roughly identified from the scans. When repeating the 2D scan with different value of the local magnetic shear ŝ, it is found that reduced ŝ lowers q_{thr} as shown in fig. 8. This is favorable, because the q range of the high density low turbulent transport regime has been widened and this regime can be achieved at lower q.

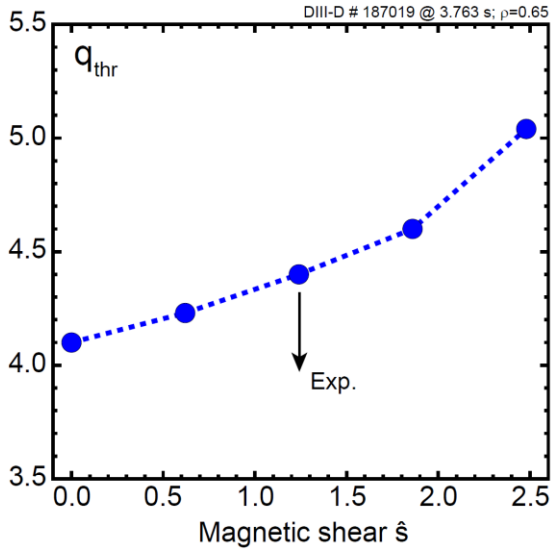

Fig. 8 The impact of local magnetic shear (ŝ) on the q threshold of access to the high density low turbulent transport regime. Black arrow indicates the experimental value used in the modeling.

Similarly, another set of 2D scans was performed by scanning β_e, instead of local q. Fig. 9(a) shows the result using experimental q value, while fig. 9(b) displays the result using double the experimental q value. In fig. 9(a), one can see that the predicted turbulent transport increases with F_p at all tested β_e values. However, the result is very different in higher q conditions as shown in fig. 9(b). When β_e is low, increased turbulent transport is still predicted at higher F_p. And finally, the high F_p low turbulent transport regime is found again at high β_e (top right corner).

Therefore, transport modeling suggests standard H-mode-type equilibrium can access the low turbulent transport regime at high density. The necessary conditions are high local q, high β and low ŝ. And this is the same regime that leads to simultaneous f_{Gr}>1 and H_{98y2}~1.5 in the high-β_P plasmas. One may notice

that q and β are two key parameters in α_{MHD} (~ $-q^2R d\beta/dr \sim d\beta_P/dr$). The underlying physics corresponding to these necessary conditions is sufficient α_{MHD} for turbulence suppression. Hence, the high-β_P scenario becomes a natural choice to pursue the goal of simultaneous high density and high energy confinement quality.

Upon revisiting the previous literature results discussed early in the introduction section, one may realize that: 1) The discharges in the ITPA database have selected q_{95} at about 3 and β_N ranging from 0.55 to 3.8 [11]; 2) The earlier high-density experiments have relatively low q_{95} and relatively low β_N (DIII-D: q_{95}~3, β_N~1.9 [12]; ASDEX Upgrade: q_{95}~4.5, β_N~1.5 [13]). Based on the physics picture revealed in this subsection, one can understand that these discharges could not get into the improved energy confinement regime at high density firstly due to the low q, and in some cases due to the low β_N as well.

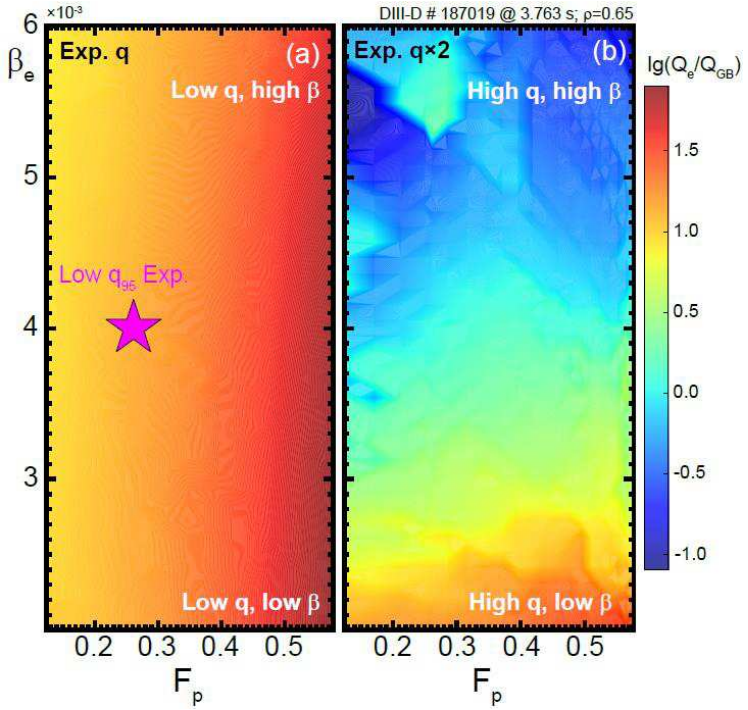

Fig. 9 2D scans of normalized electron turbulent heat flux on different plasma parameters based on the profiles shown in fig. 5(f)-(g). X-axis is F_p. Y-axis is β_e. Color coding shows $lg(Q_e/Q_{GB})$, i.e. $\log_{10}(Q_e/Q_{GB})$. (a) Experimental local q; (b) Doubled experimental local q. (a) and (b) share the same color coding. Magenta stars indicate the experimental point.

3. EAST modeling and experimental results

As discussed in the introduction section, EAST high-β_P plasmas have no ITBs at large radius, despite the similar q_{95} and β_P compared with the parameters of DIII-D high-β_P plasmas. It is important to understand the limiting factors in the EAST experiments. Is it a turbulent transport issue or because of insufficient heating power? One can use modeling to develop an approach to increase the pressure gradient at mid-radius, and then have experimental validation on the machine. In this section, predict-first transport modeling and experimental results on EAST will be presented to show the progress in understanding the limiting physics and in overcoming those limits to improve the plasma performance in the experiment.

3.1 Gyrokinetic modeling in understanding turbulence behaviors

Table 2 Major CGYRO input parameters based on EAST #81481 at 5.3 s [40]

r/a	0.676	n_i/n_e	0.8	a/L_{Ti}	0.935	a/L_{ni}	0.576
R/a	4.212	n_C/n_e	0.0333	a/L_{TC}	0.935	a/L_{nC}	0.576
q	3.027	T_i/T_e	0.726	a/L_{Te}	1.533	a/L_{ne}	0.576
$\hat{s}$	1.514	T_C/T_e	0.726	β_e	0.00209	Mach	0.0147
shift	-0.177	Z_{eff}	2.0				

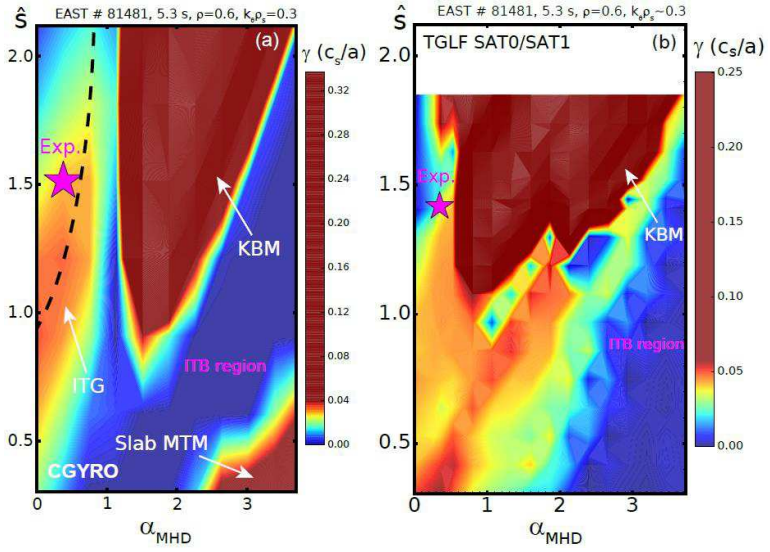

Fig. 10 2D scans of linear growth rate of most unstable turbulent instability versus α_{MHD} and magnetic shear ($\hat{s}$) Magenta star shows the experiment data point. (a) Performed by CGYRO code. Three major instabilities are indicated with labels. Black dashed line highlights the ridge of the ITG instability mountain; (b) Performed by TGLF code using saturation rule SAT-1. Different color coding in (a) and (b).

The CGYRO code [39] is employed to investigate the dominant turbulent instability at mid-radius in a typical high-β_P discharge (#81481) on EAST. This discharge has centrally peaked T_e profiles (no ITB at large radius) and β_P~2.0. The β_P value is similar to some of the DIII-D cases with large-radius ITBs. Experimental profiles of this EAST discharge can be found in the previous publication [40] (fig. 5). Input parameters of CGYRO modeling are listed in table 2. Full gyrokinetic treatment for both electron and ion species, exact shaping parametrization based on the experimental equilibrium, electromagnetic effects $\delta A_{||}$ and $\delta B_{||}$ are enabled in the modeling. Here, $\delta A_{||}$ and $\delta B_{||}$ are the parallel part and the transverse (compressional) part of the magnetic vector potential of the turbulent fluctuations, respectively. Linear analysis shows that the dominant instability at ρ=0.6 is the ITG mode. A 2D scan of magnetic shear ($\hat{s}$) and α_{MHD} has been used, previously, to illustrate the formation of the large-radius ITB in DIII-D high-β_P experiment [41]. Fig. 10(a) shows the result of a similar 2D scan based on the EAST experimental data described above. In both results, kinetic ballooning mode (KBM) instability mountain is identified. There are two major differences between the DIII-D result and the EAST result. In fig. 10(a), the EAST experimental point locates at the low gradient (α_{MHD}) side of the instability mountain (1st stability regime), while the DIII-D experimental point can access the high gradient side (2nd stability regime) [41]. Another major difference is the presence of the ITG instability mountain near the EAST experimental point in fig. 10(a). The experimental point is located in

the low gradient side of the ITG mountain. This means that an effort to increase the pressure gradient, e.g. by increasing the heating power, would suffers higher turbulent transport. This modeling result elucidates the challenge that the EAST experiment faces when trying to develop an ITB at large radius. The EAST case in fig. 10(a) shows slab micro-tearing mode (MTM) predicted in the high α and low $\hat{s}$ regime. This mode has been identified in some well-developed ITB discharges on DIII-D, and is not expected to cause large transport loss [42]. Therefore, it is likely not an obstacle for ITB development on EAST. Fig. 10(b) shows similar 2D scans using TGLF code for comparison. Using saturation rules SAT-0 [43] and SAT-1 [44] gives the same growth rates. Despite the differences in details, the lower physics fidelity of quasilinear gyro-fluid modeling (TGLF) captures the main physics of turbulence suppression by strong α_{MHD}, as demonstrated in the higher physics fidelity of gyro-kinetic modeling (CGYRO). Note that the present version of TLGF cannot model MTM since the eigen-function of MTM has a complex structure. Although using saturation rule SAT-2 predicts slightly different linear growth rates, the result still shows a KBM instability mountain and low growth rates at high α_{MHD}, i.e. 2nd stability regime. Therefore, such gyro-fluid modeling can be used for plasma core transport evaluation in the high-β_P plasmas with less required resources. A well-organized review paper on the main quasilinear transport models can be found in [45] to clarify the levels of turbulent transport modeling fidelity.

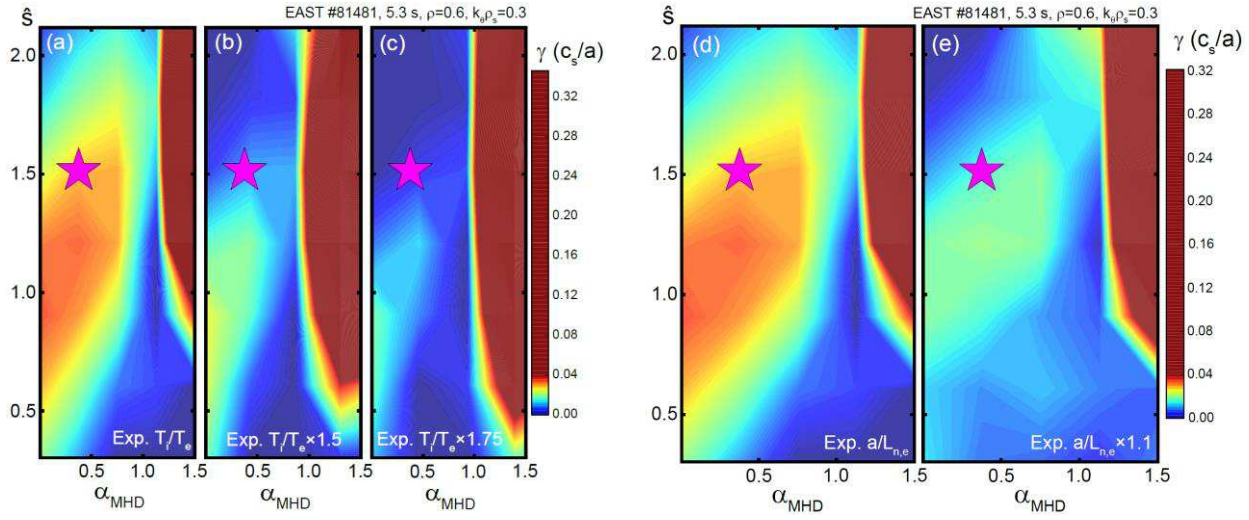

Fig. 11 Two sets of 2D scans of linear growth rate versus α_{MHD} and magnetic shear ($\hat{s}$). (a)-(c) show change of the ITG mountain at different T_i/T_e. (a) Experimental T_i/T_e value; (b) Experimental T_i/T_e×1.5; (c) Experimental T_i/T_e×1.75. (d) and (e) display change of the ITG mountain at different density gradient length (electron and impurity). (d) Experimental $a/L_{n,e}$ value; (e) Experimental $a/L_{n,e}$×1.1. Magenta stars indicate the experiment point in the $\hat{s}$-α_{MHD} panel.

CGYRO modeling also provides insight into what might be effective approaches to deal with the ITG mountain. Two approaches are identified. One is increasing T_i/T_e, which is illustrated in fig. 11(a)-(c). One can see that the ITG mountain decreases as T_i/T_e increases in the simulations. The experimental value of T_i/T_e in the EAST case is 0.73. When the value of T_i/T_e increases to a DIII-D similar level, i.e. 75% higher, the ITG instability around the experiment point almost disappears, as shown in fig. 11(c). This result suggests some ion heating power (NBI and ion cyclotron radio frequency (ICRF)) in the early phase of experiment could be helpful. Also note that higher T_i/T_e may expands the region of unstable KBM to lower shear. The other approach is increasing particle density gradients. There are multiple ways to vary density

gradients while keeping neutrality ($dn_e/dr=dn_i/dr+Z_{imp}dn_{imp}/dr$). After a few tests, increasing n_e gradient along with impurity density gradient shows the most efficient way, meaning large ITG suppression for small increase of density gradients. In this modeling, carbon is used as the main impurity. This is to be consistent with the original equilibrium from the previous work [40]. Comparing fig. 11(d) and 11(e), one can see a 10% increase in the $a/L_{n,e}$ ($\sim\nabla n_e/n_e$) (together with a 50% increase in the carbon density gradient $a/L_{n,C}$ to keep neutrality), will greatly reduce the growth rate of the ITG turbulence. Note that this corresponds to assuming all needed electron density gradient change comes from the contribution of carbon particles, i.e. this effect could be obtained by carbon impurity injection.

A recent theoretical study [46] on the turbulence suppression by strong density gradients points out that higher F_p (same definition as in section 2), higher Z_{eff}, and higher impurity density gradient have positive effects on reducing the turbulent heat flux and particle flux, according to nonlinear GENE [47] modeling (fig. 15 in [46]). The physics revealed in the paper is very general and can be applied to either an ITB or the edge pedestal, either tokamak configuration or stellarator configuration. The theoretical results reinforce the approaches discussed above to improve the performance of the EAST high-β_P plasmas.

3.2 Gyro-fluid modeling for profile predictions

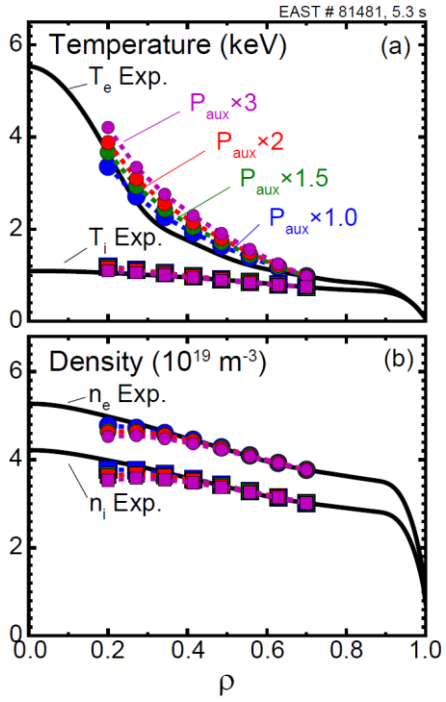

Fig. 12 Predictions of (a) temperature and (b) density profiles using TGYRO code based on the EAST high-β_P equilibrium. Different color indicates different auxiliary power in the modeling. Blue: experimental P_{aux}; Green: Experimental P_{aux}×1.5; Red: Experimental P_{aux}×2; Magenta: Experimental P_{aux}×3. Black lines show experimental profiles of T_e, T_i in (a) and n_e, n_i in (b).

In this subsection, the results of gyro-fluid modeling are discussed. This modeling effort aims to understand and predict how much the EAST profiles would improve if new experiments were to be carried out following the guidance of the gyrokinetic modeling results discussed in the previous subsection. The TGYRO code [48] is employed for profile predictions, using TGLF SAT-0 with electromagnetic effects enabled. The reason for using the SAT-0 saturation rule, instead of more recent ones, is due to the fact

that it gives reasonable agreement with the measured profiles, as shown in fig. 12, while generally poor convergence is obtained when using other saturation rules in this particular EAST equilibrium. The simulation domain is between ρ=0.2 and 0.7. The main focus of this investigation is the profile change at mid-radius. Both T_e and T_i along with n_e are predicted, while n_i is calculated based on the requirement of quasi-neutrality.

The first test, beyond the validation against the experimental profile data, is a power scan. This is to answer the question of how much of an increase in auxiliary power is needed to improve the performance of the EAST high-β_P plasmas. In the experiment, the total auxiliary power from lower-hybrid wave (LHW) and electron cyclotron heating (ECH) is about 3.2 MW. All external power goes to electrons, and mostly deposits near the magnetic axis. The heating profile is shown in fig. 13(a). In the modeling, increasing the auxiliary power by up to a factor of 3 only results in a small increase of the predicted T_e, and there is almost no change in T_i (fig. 12(a)). The predicted densities even slightly decrease at high power (fig. 12(b)). This is consistent with the finding from the gyrokinetic modeling discussed in subsection 3.1 that turbulence would clamp the profiles at mid-radius. Simply adding more auxiliary heating power is not sufficient to improve the plasma performance.

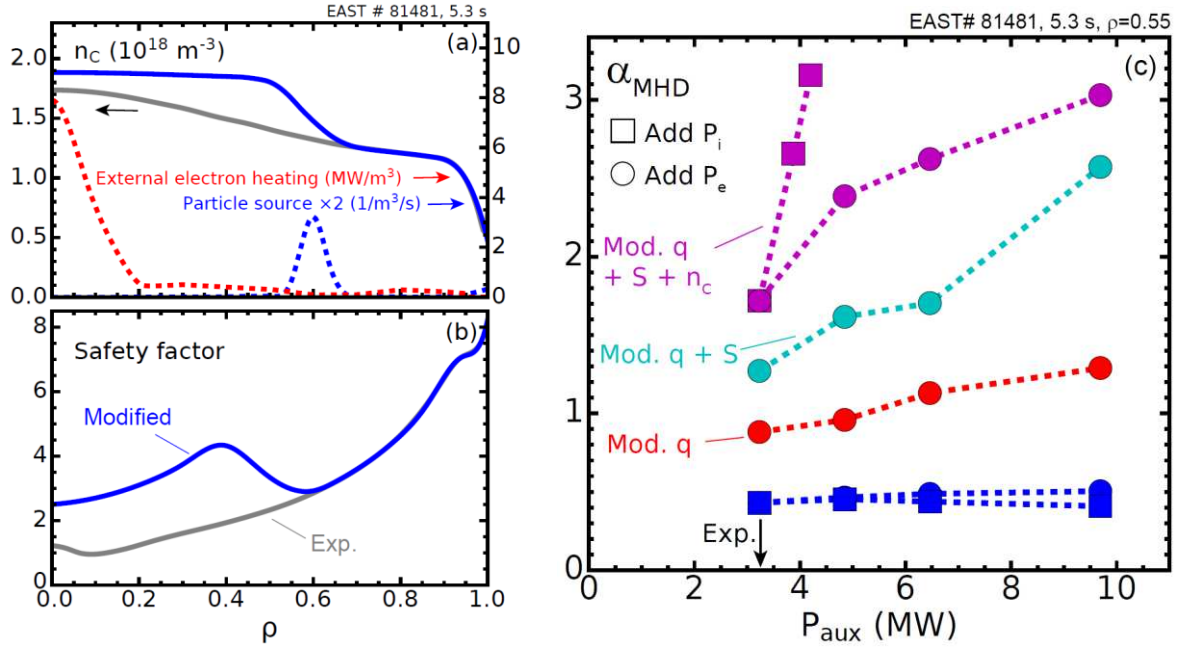

Fig. 13 (a) Experimental n_C profile in gray; Modified n_C with ITB-like higher gradient in blue; Additional particle source in the modeling in blue dashed line; External electron heating power in red dashed line. (b) Experimental q-profile in gray; Modified q-profile with reversed magnetic shear in blue. (c) Predicted α_{MHD} at ρ=0.55 versus P_{aux} in different modeling conditions. Blue: experimental condition; Red: modified q-profile from (b); Cyan: extra particle source from (a) and modified q-profile from (b); Magenta: extra particle source and modified n_C profile from (a) and modified q-profile from (b); Circles show power scans with added electron heating power; Squares indicate power scans with added ion heating power.

Next, TGYRO modeling is used to test other possible discharge optimizations, with the results shown in fig. 13(c). For simplicity, only the resulting changes in α_{MHD} (~∇p, pressure gradient) at ρ=0.55 for each scan are shown. Connecting with the previous analysis, blue circles represent the power scan results described in fig. 12. Again, very little change of α_{MHD}, i.e. ∇p, is observed when increasing P_{aux} up to ×3.

However, the situation can be improved if new optimizations are considered in the modeling, such as reducing the magnetic shear, increasing the particle source, and steepening the impurity density profile, as shown in fig. 13.

Lower magnetic shear is usually a favorable approach to establish advanced scenarios with reduced turbulent transport. In subsection 3.1, the gyrokinetic modeling results showed that the ITG instability mountain near the experimental point is mainly localized at $\hat{s}$>0.5 and low α_{MHD}. An external off-axis current drive injection, such as additional LHW current drive (LHCD), electron cyclotron current drive (ECCD), or even a transient increase of the inductive current would be beneficial to reduce the magnetic shear at mid-radius. Note that an increase of inductive current also provides transient off-axis current density as inductive current moves from plasma periphery to the core in τ_R time scale. The experimental q-profile and a modified q-profile with lower magnetic shear at large radius are shown in fig. 13(b). A TGYRO power scan with this modified q-profile was performed, and the results are shown in red in fig. 13(c). Clearly, lower magnetic shear enables higher α_{MHD} at the experimental heating power and amplifies the predicted increase in α_{MHD} with higher heating power.

In addition to the q-profile with low magnetic shear, adding a particle (electron) source in the modeling gives a further boost to the predicted α_{MHD} at mid-radius, as shown in cyan in fig. 13(c). The artificial Gaussian-like particle source is localized near ρ=0.6 (fig. 13(a)), mimicking a somewhat 'optimistic' pellet injection penetration. Direct particle source increases the predicted density gradient at mid-radius. Due to the physics discussed in section 2 (DIII-D analysis) and in subsection 3.1 (EAST gyrokinetic modeling), the increased density gradient not only would suppress the ITG turbulence, but also would amplify the α-stabilization effect, leading to ITB formation. At high power, the TGYRO modeling suggests an α_{MHD} above 2. Note that α_{MHD} above 2 is on the other side of the KBM mountain, i.e. in the ITB region, as illustrated in fig. 10(a). The predicted profiles indeed show ITB structures.

Since the impurity (carbon) profile is not predicted in this work, a set of power scans is performed with a modified carbon density profile in addition to the modified q-profile and additional particle source. The modification increases the carbon density gradient at mid-radius as shown in fig. 13(a). This modified carbon density profile could be considered as the result of an impurity pellet deposited at mid-radius. Alternatively, it could be considered as the effect of a developing impurity density ITB (similar to the DIII-D example in fig. 2(j)). The results shown in magenta circles in fig. 13(c) suggest a favorable impact on the pressure gradient. α_{MHD}>2 is predicted at lower auxiliary power than the results with the experimental carbon density profile.

Finally, a power scan is carried out by adding ion heating power, instead of electron heating, to the experimental heating power. The added ion heating power profile is central-peaked, having the same shape of the electron heating power. The results are shown in squares in fig. 13(c). With all optimizations, it turns out that additional ion heating power can significantly increase α_{MHD} at even lower total power level. This implies a desirable choice would be to add NBI and ICRF power in the heating mix of the EAST experiments. However, the situation would be different if without optimizations. Experimental analysis from WEST tokamak shows that insufficient ion heating may play a role in limiting T_i in plasma core [49]. This is explained by a value of τ_{ei}/τ_E close 1, where τ_{ei} is the volume averaged electron-ion collisional heat exchange time. Although the EAST case has experimental τ_{ei}/τ_E about 0.83, which is also possibly associated with insufficient ion heating in the core, it is worth pointing out that in the EAST case, adding 7 MW of additional ion heating power in the modeling has little change of the predicted T_i gradient at

mid-radius (blue squares in fig. 13(c)). The new set of power scan experiment on EAST will be further discussed in the next subsection. In the modeling, the benefit of adding ion heating power significantly reduces without making the three optimizations discussed above.

The effects of the optimizations described above have been further investigated in a time-dependent manner. This enables to model the effect of a brief plasma current ramp-up for reducing the magnetic shear at mid-radius, including the engineering constraints of the EAST superconducting coils. This modeling is performed using the FASTRAN code [50] with TGLF as the turbulent transport model and the saturation rule SAT-2 is used. Other saturation rules are also tested with little change. Initial input comes from EAST #101473 at 3.58 s, which includes 2.4 MW RF power plus 0.74 MW NBI power for electron heating and 1 MW NBI power for ion heating. The heating profiles are shown in fig. 14(a). Three types of actuators are designed for optimization: 1) I_p ramp-up rate: 0.5 MA/s; 2) Gaussian-like particle source profile centered at ρ=0.75 with height at 1.4×10^{21} m^{-3}/s and half-height-full-width of 0.3 in ρ; 3) Z_{eff} increases from 2.0 to 2.8 around ρ=0.6, assuming the additional particle source comes from carbon impurities. More details of this modeling work will be reported in a separated paper. In fig. 14(b), the predicted T_i profiles are shown to highlight the main conclusions. One can see that a single actuator, either extra particle source for higher density gradient at mid-radius or plasma current ramp-up for transiently reduced magnetic shear, has limited impact on improving the pressure gradient at mid-radius. Combining particle source and higher Z_{eff} or current ramp-up has slightly better results. The strongest effect comes from the combination of the three actuators as shown in magenta in fig. 14(b).

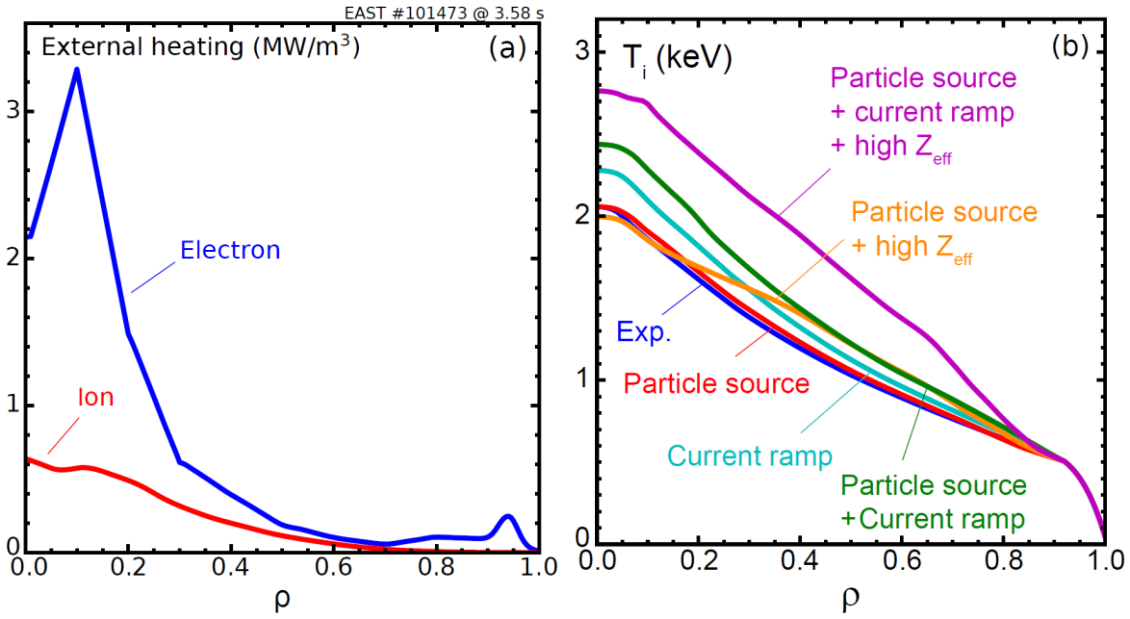

Fig. 14 (a) External heating profiles used in the FASTRAN modeling. Electron heating in blue; Ion heating in red; (b) Predicted T_i profiles in FASTRAN based on the EAST conditions and with additional actuators. Blue line shows the prediction with experimental conditions. Results of adding single actuator are shown in red for extra particle source and in cyan for additional current ramp-up. Results of adding two actuators are illustrated in green for extra particle source plus current ramp and in orange for extra particle source plus higher Z_{eff}. Magenta line displays the result of three actuators: extra particle source plus current ramp and higher Z_{eff}.

An EAST experiment proposal was therefore developed, based on the guidance from all the modeling results, emphasizing the application of a combined plasma current ramp-up and impurity injection.

3.3 Theory-guided experiments to increase the ion temperature on EAST

In this subsection, a series of EAST experiments is presented to test the modeling results. The first test is a power scan, since the available auxiliary power in EAST has been further developed in recent years. The experiment uses a mix of auxiliary powers, including from NBI, ECH, LHW, and ICRF. As shown in fig. 15(a) and 15(b), two of the lower power discharges use RF power only with total power at 4.7 MW and 5.8 MW, respectively. There are a few NBI blips in these discharges to enable diagnostic measurements. Continuous NBI heating is added in the two higher power discharges, with total power at 8.5 MW and 10.9 MW. One of the beam line drops out unexpectedly in #129153 around t=8.8 s, thus creating an additional power level at 9.65 MW. The plasma current is 300 kA in all these discharges. It corresponds to a q_{95} value between 9.0 and 10.5, depending on the plasma β. The line-averaged density is 80% of the Greenwald value for the two lower power discharges and is 90-95% for the two higher power discharges, as shown in fig. 15(c). Fig. 15(d) displays time evolutions of the on-axis ion temperature (T_{i0}) measured by the X-ray crystal spectrometer [51]. As one can see, T_{i0} responds weakly to the increased heating power in the phase between 6.4 s and 12.4 s. The measurements show about 30% higher T_{i0} at doubled the heating power (comparing blue and orange cases). This scan confirms experimentally the limited effect of simply increasing the heating power that was predicted in the modeling discussed earlier. Thus, it is important to incorporate other optimizations for turbulence suppression.

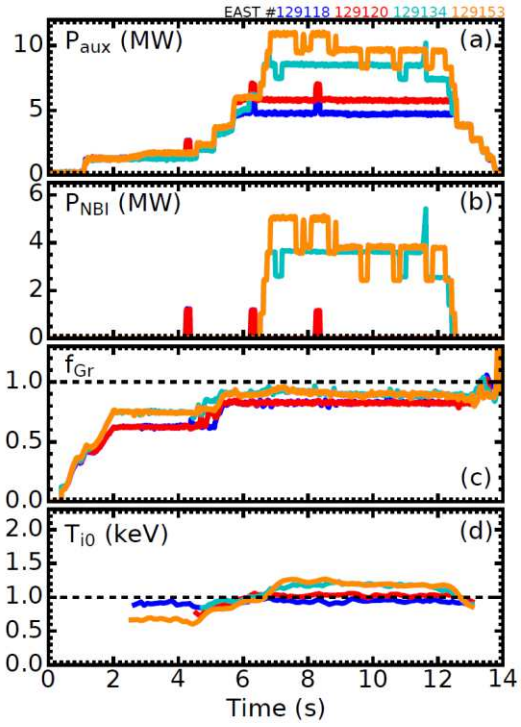

Fig. 15 Time histories of EAST discharges. (a) Total auxiliary power; (b) NBI power; (c) normalized line-averaged density to the Greenwald value; (d) ion temperature measured on magnetic axis.

In a following set of tests, the experiment followed the guidance from the previous transport modeling results. The key results are shown in fig. 16. Discharge #129138 is the reference discharge, with I_p=300 kA, f_{Gr}~0.9 and P_{aux}=9.5 MW. These parameters are kept constant in this set of discharges, except for one of the beam lines dropping unexpectedly at 9.3 s in #129139. The first test is adding argon (Ar) particles via

the supersonic molecular beam injection (SMBI) system [52] in #129139. A single pulse of Ar was injected into the plasma with 100 ms pulse length at 7.0 s (fig. 16(a)). The measured T_{i0} shows a brief increase and soon decreases to the same value of the reference case as shown in fig. 16(c). In the next discharge #129140, a 2nd I_p ramp-up with additional 50 kA in 0.5 s was added at 7.0 s. This change has noticeable improvement in T_{i0}. Unlike #129139, the improved T_{i0} did not return to the reference level. In #129141, an additional 100 ms pulse of Ar was added via a 2nd SMBI injector, therefore, the amount of Ar impurity doubled. This discharge achieved the highest T_{i0} in the experiments. Similar to #129140, the ion temperature did not return to the reference level, and a large improvement in T_{i0} was still maintained after several seconds of discharge duration.

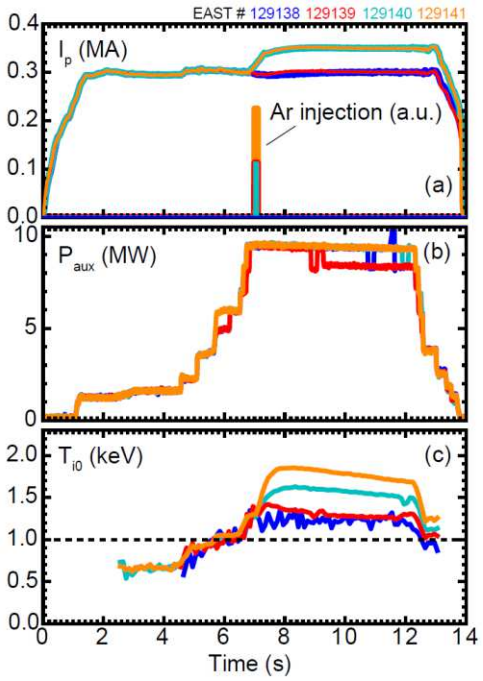

Fig. 16 Time histories of EAST discharges. (a) Plasma current (top), Ar injection (bottom); (b) Auxiliary power (total power); (c) Ion temperature measured on magnetic axis.

The consecutive discharges #129138-129141 demonstrated effective T_{i0} improvement when Ar injection and a brief I_p ramp-up were applied together, while a very weak response in T_{i0} was observed with Ar injection alone. However, a remaining question needs to be addressed in order to disentangle the effects of I_p ramp-up and Ar injection. That is whether the I_p ramp-up alone can trigger a noticeable T_{i0} increase in the same plasma conditions. Fig. 17 shows the time histories of discharge #129147, with same basic settings of discharge #129141 in fig. 16, except that the Ar injection timing was delayed from 7.0 s to 8.0 s. One can see that very little increase in T_{i0} was observed when using the I_p ramp-up alone at 7.0 s, as highlighted by the gray shaded area in fig. 17. On the contrary, the Ar injection at 8.0 s created a large response in T_{i0} (cyan shaded area in fig. 17), reaching a similar T_{i0} level compared with the result in #129141.

The experimental observations are consistent with the transport modeling predictions discussed in subsection 3.1 and 3.2. With increased heating power alone, the level of T_{i0} only increased about 30%, despite a doubling of the heating power, as shown in fig. 15. On the other hand, using all the actuators suggested by the modeling results, T_{i0} increased about 85% when the heating power increased by about 50% (comparing 6.0 s and 8.0 s in #129141). Indeed, by comparing the best case (#129141) against the

reference (#129138), one can see that T_{i0} increased about 54% without adding any additional heating power between 7.0 s and 12.5 s.

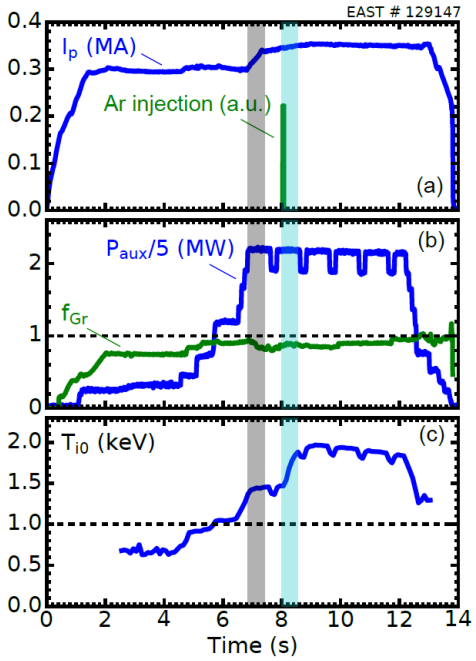

Fig. 17 Time histories of EAST discharge #129147. (a) Plasma current in blue and Ar injection in green; (b) Auxiliary power (total power) in blue and f_{Gr} in green; (c) Ion temperature measured on magnetic axis.

It is worth mentioning that EAST has previously achieved enhanced T_i by Ar injection [53]. One of the major differences between the results in that work and what has shown in this paper, is the amount of Ar used in the experiment. The previous experiment used a chain of Ar pulses for the purpose of testing radiative divertor, while the experiment described in this paper only used a short pulse to improve plasma confinement. The response in Z_{eff} is therefore significantly different. Z_{eff} increased about 0.2 after the Ar injection at 7.0 s in discharge #129141 discussed in this paper, while Z_{eff} increased about 0.9 in the radiative divertor experiment, as shown in fig. 4 of [46]. Another interesting phenomenon in the new experiments is the slow decay of T_{i0} observed in the successful discharges (fig. 16(c)). Although the decrease is not significant, e.g. from 1.85 keV to 1.68 keV in #129141 over 4 s, it still implies unclear physics in the discharges. As more detailed experimental data are being processed and analyzed by the EAST team, a better picture of the underlying physics in this experiment may emerge for future publications to discuss.

4. Summary and discussion

This paper reports the coordinated breakthroughs achieved on DIII-D and EAST for improved energy confinement at line-averaged density near the Greenwald value. On DIII-D, high-β_P experiments have pushed the operational boundary of divertor tokamaks to simultaneous f_{Gr} up to 1.25 and H_{98y2} from 1.3 to 1.7. For reference, sustained H_{98y2}~1.5 at f_{Gr}>1.1 has been achieved for 2.2×τ_R in DIII-D discharge #190904, with simultaneous increase of n_i, T_i, τ_E and the neutron rate, while with reduced toroidal rotation and T_i/T_e close to 1. Although not emphasized in this paper, this discharge also shows small ELMs and reduced divertor heat load in the high confinement and high density phase [18]. The experimental

achievement supports many attractive FPP designs all over the world that require f_{Gr}>1 and H_{98y2}>1 at the same time. Enhanced α-stabilization of turbulence transport at high density gradient, which enables the synergy between high density and high energy confinement, is proposed as the key to accessing this operational regime. Transport modeling shows fundamental differences in transport features at mid-radius between the high-β_P plasma and a low-q_{95} high-density H-mode. For the high-β_P case, a decreasing turbulent transport is predicted with higher density gradient, while for the low q_{95} H-mode case, an increasing turbulent transport with higher density gradient is predicted. Both predictions agree with the experimental observations. Further modeling explorations indicate that the favorable conditions to access the low turbulent transport regime at high density are a relatively high local q and high β. Reducing the magnetic shear is helpful for access, because it is predicted to reduce the threshold q value.

The inherent connections between the efforts of high-β_P scenario development on DIII-D and EAST include a deep understanding of the governing physics in the DIII-D results and an application of the same physics in EAST experiment. The physics insights presented in the DIII-D part of this paper and similar analysis techniques were applied to EAST high-β_P plasmas. Gyrokinetic analysis suggests that, in addition to KBM instability, ITG turbulence keeps the main ions cold and prevents these EAST plasmas from entering the 2nd stability regime at high α_{MHD}, where the ITB emerges. Higher T_i/T_e and higher density gradient by impurity injection are two approaches predicted to effectively suppress ITG turbulence. Two sets of independent gyro-fluid modeling (a set using TGYRO, and a set of time-dependent simulations using FASTRAN) were performed testing different optimizations to raise the ion temperature profile in EAST. Both modeling approaches show that a combined approach of extra particle source at mid-radius, impurity injection, and reduced magnetic shear at large radius would lead to the strongest improvement of plasma performance. Following this guidance, a nearly doubled T_i at f_{Gr}~0.9 has been achieved on EAST, using the combination of a 2nd I_p ramp-up, which possibly broadens the current profile at large radius, a short pulse of Ar injection to both inject impurity ions and additional electrons, and higher auxiliary power with more ion heating. The experiments also showed much less improvement in T_i when applying each technique separately, as was anticipated by the modeling studies. This is a successful first step towards developing large-radius ITBs in EAST long-pulse high-β_P plasmas and solving the long-standing challenge of raising the ion temperature in this regime.

Regarding the potential of the high-β_P scenario for high absolute performance, high-Q operations in ITER or an FPP have been predicted, including steady-state ITER Q=5 [54], ITER Q=10 at I_p~7.5 MA [55] and steady-state compact FPP Q~17 and 200 MWe output (colume D in table 2 of [7]) with plasma parameter matching DIII-D high β_P discharge in [56].

Acknowledgement

This material is based upon work supported by the U.S. Department of Energy, Office of Science, Office of Fusion Energy Sciences, using the DIII-D National Fusion Facility, a DOE Office of Science user facility, under Awards DE-SC0010685, DE-FC02-04ER54698, DE-AC52-07NA27344, DE-FG02-04ER54761, DE-AC02-09CH11466 and DE-SC0016154. This report was prepared as an account of work sponsored by an agency of the United States Government. Neither the United States Government nor any agency thereof, nor any of their employees, makes any warranty, express or implied, or assumes any legal liability or responsibility for the accuracy, completeness, or usefulness of any information, apparatus, product, or process disclosed,

or represents that its use would not infringe privately owned rights. Reference herein to any specific commercial product, process, or service by trade name, trademark, manufacturer, or otherwise, does not necessarily constitute or imply its endorsement, recommendation, or favoring by the United States Government or any agency thereof. The views and opinions of authors expressed herein do not necessarily state or reflect those of the United States Government or any agency thereof.

AUTHOR DECLARATIONS

Conflict of Interest

The authors have no conflicts to disclose.

DATA AVAILABILITY

The data that support the findings of this study are available from the corresponding author upon reasonable request.

References

[1] J. H. Yeom, K. Kim, Y. S. Lee, H. C. Kim, S. Oh, K. Im and C. Kessel, *Fusion Eng. Des.* **88** (2013) 742

[2] G. Zhuang, G. Q. Li, J. Li, Y. X. Wan, Y. Liu, X. L. Wang, Y. T. Song, V. Chan, Q. W. Yang, B. N. Wan *et al.*, *Nucl. Fusion* **59** (2019) 112010

[3] H. Lux, R. Kemp, R. Wenninger, W. Biel, G. Federici, W. Morris and H. Zohm, *Fusion Eng. Des.* **123** (2017) 63

[4] G. Federici, C. Bachmann, L. Barucca, W. Biel, L. Boccaccini, R. Brown, C. Bustreo, S. Ciattaglia, F. Cismondi, M. Coleman *et al.*, *Fusion Eng. Des.* **136** (2018) 729

[5] C. E. Kessel, M. S. Tillack, F. Najmabadi, F. M. Poli, K. Ghantous, N. Gorelenkov, X. R. Wang, D. Navaei, H. H. Toudeshki, C. Koehly *et al.*, *Fusion Sci. Technol.* **67** (2015) 1

[6] M. R. Wade and J. A. Leuer, *Fusion Sci. Technol.* **77** (2021) 119

[7] R. J. Buttery, J. M. Park, J. T. McClenaghan, D. Weisberg, J. Canik, J. Ferron, A. Garofalo, C. T. Holcomb, J. Leuer, P. B. Snyder *et al.*, *Nucl. Fusion* **61** (2021) 046028

[8] N. Shi, T. Slendebroek, J. T. McClenaghan, S. Ding, B. Lyons, O. Meneghini and D. Weisberg, *64th Annual Meeting of the APS Division of Plasma Physics*, **UP11.00004**, Oct. 17-21, 2022, Spokane, Washington, USA

[9] J. Wesson, *Tokamaks*, 3rd ed. (Oxford University Press, 2004)

[10] M. Greenwald, *Plasma Phys. Control. Fusion* **44** (2002) R27

[11] A. C. C. Sips, J. Schweinzer, T. C. Luce, S. Wolfe, H. Urano, J. Hobirk, S. Ide, E. Joffrin, C. Kessel, S. H. Kim *et al.*, *Nucl. Fusion* **58** (2018) 126010

[12] T. H. Osborne, A. W. Leonard, M. A. Mahdavi, M. Chu, M. E. Fenstermacher, R. La Haye, G. McKee, T. W. Petrie, E. Doyle, G. Staebler *et al.*, *Phys. Plasmas* **8** (2001) 2017

[13] P. T. Lang, W. Suttrop, E. Belonohy, M. Bernert, R. M. Mc Dermott, R. Fischer, J. Hobirk, O. J. W. F. Kardaun, G. Kocsis, B. Kurzan *et al.*, *Nucl. Fusion* **52** (2012) 023017

[14] P.T. Lang, A. Burckhart, M. Bernert, L. Casali, R. Fischer, O. Kardaun, G. Kocsis, M. Maraschek, A. Mlynek, B. Plöckl *et al.*, *Nucl. Fusion* **54** (2014) 083009

[15] H. Takenaga, N. Asakura, H. Kubo, S. Higashijima, S. Konoshima, T. Nakano, N. Oyama, G. D. Porter, T. D. Rognlien, M. E. Rensink *et al.*, *Nucl. Fusion* **45** (2005) 1618

[16] B. Unterberg, U. Samm, M. Z. Tokar, A. M. Messiaen, J. Ongena and R. Jaspers, *Fusion Sci. Technol.* **47** (2005) 187

[17] K. E. Thome. M. E. Austin, A. W. Hyatt, A. Marinoni, A. O. Nelson, C. Paz-Soldan, F. Scotti, W. S. Boyes, L. Casali, C. Chrystal *et al.*, *Plasma Phys. Control. Fusion* **66** (2024) 105018
[18] S. Ding, A. M. Garofalo, H. Q. Wang, D. B. Weisberg, Z. Y. Li, X. Jian, D. Eldon, B. S. Victor, A. Marinoni, Q. M. Hu *et al.*, *Nature* **629** (2024) 555
[19] M. Kikuchi, *Nucl. Fusion* **30** (1990) 265
[20] Y. Koide, M. Kikuchi, M. Mori, S. Tsuji, S. Ishida, N. Asakura, Y. Kamada, T. Nishitani, Y. Kawano, T. Hatae *et al.*, *Phys. Rev. Lett.* **72** (1994) 3662
[21] Y. Sakamoto, T. Fujita, S. Ide, A. Isayama, M. Takechi, T. Suzuki, H. Takenaga, N. Oyama, Y. Kamada and the JT-60 Team, *Nucl. Fusion* **45** (2005) 574
[22] A. M. Garofalo, X. Z. Gong, B. A. Grierson, Q. Ren, W. M. Solomon, E. J. Strait, M. A. Van Zeeland, C. T. Holcomb, O. Meneghini, S. P. Smith *et al.*, *Nucl. Fusion* **55** (2015) 123025
[23] S. Ding and A. M. Garofalo, *Rev. Mod. Plasma Phys.* **7** (2023) 4
[24] X. Gong on behalf of EAST Team and Collaborators, *Nucl. Fusion* **64** (2024) 112013
[25] G.M. Staebler, G. L. Jackson, W. P. West, S. L. Allen, R. J. Groebner, M. J. Schaffer and D. G. Whyte, *Phys. Rev. Lett.* **82** (1999) 1692
[26] R.J. Hawryluk, Proc. Course Held in Varenna, Italy, 27 August–8 September 1979, pp 19–46, 1981 [https://doi.org/10.1016/B978-1-4832-8385-2.50009-1]
[27] O. Meneghini, S. P. Smith, L. L. Lao, O. Izacard, Q. Ren, J. M. Park, J. Candy, Z. Wang, C. J. Luna, V. A. Izzo *et al.*, *Nucl. Fusion* **55** (2015) 083008
[28] C. Paz-Soldan and the DIII-D team, *Plasma Phys. Control. Fusion* **63** (2021) 083001
[29] G. Verdoolaege, S. M. Kaye, C. Angioni, O. J. W. F. Kardaun, M. Maslov, M. Romanelli, F. Ryter, K. Thomsen, the ASDEX Upgrade Team, the EUROfusion MST1 Team and JET Contributors, *Nucl. Fusion* **61** (2021) 076006
[30] A. M. Garofalo, X. Z. Gong, S. Ding, J. Huang, J. McClenaghan, C. K. Pan, J. Qian, Q. L. Ren, G. M. Staebler, J. Chen *et al.*, *Plasma Phys. Control. Fusion* **60** (2018) 014043
[31] G. R. McKee, R. J. Fonck, D. K. Gupta, D. J. Schlossberg, M. W. Shafer and R. L. Boivin, *Rev. Sci. Instrum.* **77** (2006) 10F104
[32] M. T. Kotschenreuther, X. Liu, D. R. Hatch, S. M. Mahajan, M. J. Pueschel, M. Halfmoon, I. J. McKinney, P. Xanthopoulos, A. Garafolo, J. McClenaghan *et al.*, *61st Annual Meeting of the APS Division of Plasma Physics*, **UP10.00020**, Oct. 21-25, 2019, Fort Lauderdale, Florida, USA
[33] X. Litaudon, *Plasma Phys. Control. Fusion* **48** (2006) A1
[34] R. P. Seraydarian and K. H. Burrell, *Rev. Sci. Instrum.* **57** (1986) 2012
[35] W. M. Solomon, P. A. Politzer, R. J. Buttery, C. T. Holcomb, J. R. Ferron, A. M. Garofalo, B. A. Grierson, J. M. Hanson, Y. In, G. L. Jackson *et al.*, *Nucl. Fusion* **53** (2013) 093033
[36] S. Ding, A. M. Garofalo, M. Knolker, A. Marinoni, J. McClenaghan and B. A. Grierson, *Nucl. Fusion* **60** (2020) 034001
[37] G. M. Staebler, J. E. Kinsey and R. E. Waltz, *Phys. Plasmas* **12** (2005) 102508
[38] G. M. Staebler, E. A. Belli, J. Candy, J. E. Kinsey, H. Dudding and B. Patel, *Nucl. Fusion* **61** (2021) 116007
[39] J. Candy, E. A. Belli and R. V. Bravenec, *J. Comput. Phys.* **324** (2016) 73
[40] M. Q. Wu, G. Q. Li, J. P. Qian, X. Z. Gong, A. M. Garofalo, J. L. Chen, Q. L. Ren, X. Gao, K. Li, X. Zhu *et al.*, *Nucl. Fusion* **59** (2019) 106009
[41] L. Wang, H. Q. Wang, S. Ding, A. M. Garofalo, X. Z. Gong, D. Eldon, H. Y. Guo, A. W. Leonard, A. W. Hyatt, J. P. Qian *et al.*, *Nat. Commun.* **12** (2021) 1365

[42] X. Jian, C. Holland, J. Candy, E. Belli, V. Chan, A. M. Garofalo and S. Ding, *Phys. Rev. Lett.* **123** (2019) 225002
[43] J. E. Kinsey, G. M. Staebler and R. E. Waltz, *Phys. Plasmas* **15** (2008) 055908
[44] G. M. Staebler, J. Candy, N. T. Howard and C. Holland, *Phys. Plasmas* **23** (2016) 062518
[45] G. Staebler, C. Bourdelle, J. Citrin and R. Waltz, *Nucl. Fusion* **64** (2024) 103001
[46] M. Kotschenreuther, X. Liu, S. M. Mahajan, D. R. Hatch and G. Merlo, *Nucl. Fusion* **64** (2024) 076033
[47] F. Jenko, W. Dorland, M. Kotschenreuther and B. N. Rogers, *Phys. Plasmas* **7** (2000) 1904
[48] J. Candy, C. Holland, R. E. Waltz, M. R. Fahey and E. Belli, *Phys. Plasmas* **16** (2009) 060704
[49] P. Manas, J. F. Artaud, C. Bourdelle, V. Ostuni, J. Morales, J. Citrin and the WEST Team, *Nucl. Fusion* **64** (2024) 036011
[50] J. M. Park, M. Murakami, H. E. St. John, L. L. Lao, M. S. Chu and R. Prater, *Comput. Phys. Commun.* **214** (2017) 1
[51] B. Lyu, J. Chen, R. J. Hu, F. D. Wang, Y. Y. Li, J. Fu, Y. C. Shen, M. Bitter, K. W. Hill, L. F. Delgado-Aparicio *et al.*, *Rev. Sci. Instrum.* **87** (2016) 11E326
[52] X. L. Yuan, J. G. Li, J. H. Wu, J. H. Li, Y. Chen, H. D. Zhuang, Y. Zhou, X. W. Zheng and J. S. Hu, *Fusion Eng. Des.* **134** (2018) 62
[53] X. Yang, X. Gong, J. Qian, Y. Jin, P. Manas, P. Li, C. Bourdelle, Y. Chu, B. Zhang, Y. Chen *et al.*, *Nucl. Fusion* **64** (2024) 016030
[54] J. McClenaghan, A. M. Garofalo, L. L. Lao, D. B. Weisberg, O. Meneghini, S. P. Smith, B. C. Lyons, G. M. Staebler, S. Ding, J. Huang *et al.*, *Nucl. Fusion* **60** (2020) 046025
[55] S. Ding, A. M. Garofalo, J. McClenaghan, H. Wang, C. Chrystal, D. Eldon, D. B. Weisberg, L. Wang, X. Gong, J. Qian *et al.*, *28th IAEA Fusion Energy Conference*, **EX/1-3R**, May 10-15, 2021, Remote conference
[56] J. Huang, A. M. Garofalo, J. P. Qian, X. Z. Gong, S. Ding, J. Varela, J. L. Chen, W. F. Guo, K. Li, M. Q. Wu *et al.*, *Nucl. Fusion* **60** (2020) 126007